ACS OMEGA

Open Access

http://pubs.acs.org/journal/acsodf

Article

Influence of Gold Nanoparticles on eNOS Localization in Gill Tissues: Advancements in Immunofluorescence Techniques

Ramla Gary, Manel Ben Salah, Taoufik Soltani, Patrizia Formoso, and Souhaira Hbaieb*

Cite This: *ACS Omega* 2024, 9, 49530−49538

Read Online

ACCESS | Metrics & More | Article Recommendations

ABSTRACT: This study optimizes immunofluorescence techniques using gold nanoparticles (AuNPs) to improve visualization of endothelial nitric oxide synthase (eNOS) in gill tissue. Two types of AuNP dispersions, stabilized in phosphate buffered saline (PBS) and citrate buffer (CB), were evaluated for their imaging performance. AuNPs suspended in PBS provided significantly better optical contrast due to uniform distribution and effective tissue attachment, whereas citrate-suspended AuNPs exhibited aggregation, resulting in reduced contrast. These results highlight the influence of suspension media on AuNP performance, particularly in balancing fluorescence signals to improve contrast. The PBS suspension allowed clearer visualization of eNOS, highlighting the role of AuNP compatibility in improving immunofluorescence results. This study highlights the importance of strategic selection of AuNP dispersions in contrast agent design and provides insights for advanced imaging applications where sensitivity and accurate localization of biomolecules are essential. By refining the use of AuNPs as contrast enhancers, this approach offers potential improvements in bioimaging accuracy, facilitating more precise visualization in complex tissue environments.

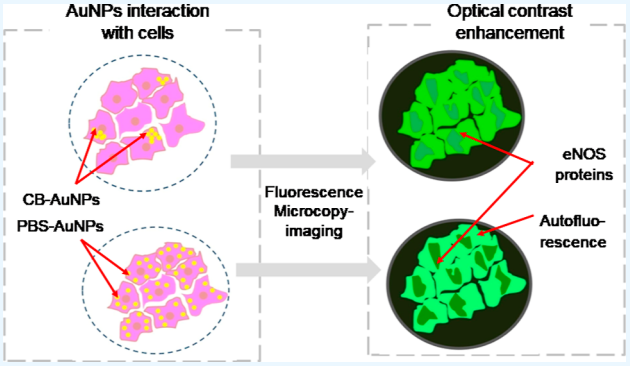

1. INTRODUCTION

Immunofluorescence is a widely used technique in biology to visualize specific biological molecules, such as proteins or antigens, using fluorescently labeled antibodies. This method relies on the specific binding of antibodies to antigens, allowing the detection and localization of various target biomolecules within cell or tissue. Despite efforts to reduce background signal (autofluorescence) through techniques such as decreasing fluorophore concentration and extensive washing, nonspecific binding can still increase background noise. In addition, intrinsic signals from certain cellular components can interfere with the detection of specific fluorescent signals, posing a challenge to accurate imaging.[1−4]

Moreover, intrinsic signals naturally emitted by certain cellular components, while often prominent in the blue region of the spectrum, can extend beyond this region and potentially interfere with the detection of specific fluorescent signals.[5,6] This inherent autofluorescence poses a significant challenge to immunofluorescence experiments and necessitates the search for more effective contrast agents.[7] Gold nanoparticles (AuNPs) have emerged as promising candidates for improving bioimaging techniques due to their unique optical properties and lower toxicity compared to other plasmonic materials.[8,9] In fluorescence-based imaging techniques, the surface plasmon resonance (SPR) of AuNPs allows them to interact with fluorophores through various mechanisms, including both radiative and nonradiative processes.[10−12] Förster Resonance Energy Transfer (FRET), a radiative process, occurs when conditions such as proximity, spectral overlap between the emission spectrum of the fluorophore (or absorption spectrum, since both AuNPs and fluorophores can act as donors and acceptors) and the SPR absorption spectrum of the AuNPs, and dipole−dipole interactions are met.[5,13,14] By introducing AuNPs into biological tissues, these mechanisms can be exploited to significantly enhance optical contrast, thereby improving the precision of target protein localization. This multifaceted enhancement optimizes the immunofluorescence technique, making it a more powerful tool for the visualization of specific biomolecules (Figure 1). The interaction between AuNPs and fluorophores is critical for this enhancement but is highly dependent on parameters such as the interaction of AuNPs with biological tissues, where their physicochemical properties (size, shape and surface charge) play a key role.[15,16] Since nanoparticle-cell interactions primarily occur at the

Received: August 11, 2024
Revised: November 11, 2024
Accepted: November 19, 2024
Published: November 28, 2024

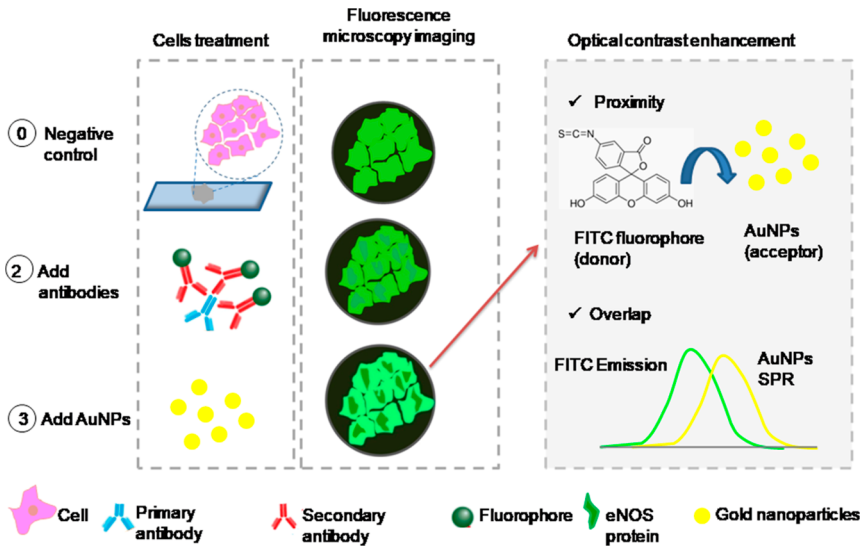

Figure 1. Immunofluorescence optimization using gold nanoparticles (AuNPs) as optical contrast enhancers.

nanoparticle-cell interface, a thorough understanding of how the surface properties of AuNPs influence their interactions with cells is crucial for their therapeutic, diagnostic, and bioimaging applications.[17,18] Furthermore, the effect of buffer solutions on the surface characteristics and colloidal stability of AuNPs is critical,[19] particularly for their use in bioimaging techniques such as immunolocalization. Despite the importance of buffer solutions, their influence on immunolocalization performance has not been systematically investigated.

This study aims to determine the optimal dispersion conditions for gold nanoparticles in the immunolocalization of specific proteins. Using gills as a model sample and endothelial nitric oxide synthase (eNOS) as a target protein, we investigated the effects of two different AuNP suspension solutions on immunofluorescence performance. This approach is designed to improve our understanding of the interactions between AuNPs, fluorophores, and biological tissues, with the ultimate goal of optimizing immunofluorescence protocols for applications in biology and medicine.

2. MATERIALS AND METHODS

2.1. Methods. Zeta potential (ZP), hydrodynamic diameter (D_H) and polydispersity index (PDI) measurements of AuNPs were performed using the Zetasizer Nano-ZS (Malvern Instruments Ltd. UK). Clear disposable folded capillary cells (700 μL) with built-in electrodes capable of both D_H and ZP measurements were used. Each data point for ZP was an average of at least 50 runs of 10 s each. Malvern Zetasizer software version 7.12 was used to analyze the collected data using monomodal acquisition and fitting according to the Smoluchowski theory. D_H and PDI were determined from the autocorrelation function using the "general purpose mode" and a backscatter detection system at 173°. For each sample, ZP, D_H, and thus PDI were measured three times and expressed as the mean ± standard deviation. The absorption spectra of the two solutions of AuNPs were measured using a UV−vis−NIR spectrophotometer AVASPE-2048 (Avantes, Apeldoorn, NL).To determine the morphology and chemical composition of AuNPs, transmission electron microscopy (TEM) and X-ray energy dispersive spectroscopy (EDX) were performed using a JEOL JEM-1400 Plus electron microscope (JEOL Ltd., Tokyo, Japan) at 80 kV. Ten μL of diluted AuNPs solution was dropped onto carbon-coated copper grids (G300 Cu, Electron Microscopy Sciences, Hatfield, PA). The solution was allowed to evaporate prior to performing microscopy. SEM images of AuNPs treated tissues were taken after removing the coverslip and applying the conductive coating. Experiments were performed using a field emission scanning electron microscope (FESEM)—FEI Quanta 200 under the following operating conditions: HV: 20Kev, Signal: BSE (Back Scattered Electron), and working distance: 11 mm.

2.2. Gold Nanoparticles. For this study, two commercially available solutions of AuNPs purchased from Sigma-Aldrich were used. The pH of both AuNPs dispersions was 7, with an optical density of 1 and a particle concentration of ~$3.5 \times 10^{+10}$ particles mL^{-1}, with a core size in the range of 37−43 nm and a mean hydrodynamic diameter of approximately 48−56 nm. The first solution contained AuNPs stabilized in 0.1 mM phosphate buffer saline (PBS) (PBS-AuNPs), while the second solution contained AuNPs suspended in citrate buffer (CB-AuNPs).

2.3. Tissue Samples. Gill samples from lungfish *Protopterus annectens* (n = 3) were excised and rinsed in PBS. Samples were then fixed in M.A.W. solution (methanol/acetone/water = 2:2:1), dehydrated in graded ethanol (90% and 100%) cleared in xylol, embedded in Paraplast (Sigma-Aldrich) and serially sectioned at 8 μm. Sections were placed on Superfrost Plus slides (Menzel-Glaser, Braunschweig, Germany), deparaffinized in xylene, and rehydrated in an alcohol gradient. Several sections were stained with hematoxylin−eosin for general assessment of tissue structure.

2.4. Immunofluorescence Procedure. Tissue sections, obtained and prepared as described above, were rinsed in tris-buffered saline (TBS). Slides were pretreated separately with AuNPs suspended in PBS and citrate buffer at 4 °C. The sections were then incubated again overnight at 4 °C with a rabbit polyclonal primary antibody directed against eNOS (anti-eNOS) (Sigma-Aldrich, 1:100). Incubation with AuNPs and immunofluorescence procedures were performed at room temperature. After primary antibody incubation, the slides were washed in tris-buffered saline (TBS) (3 × 10 min) and incubated with antirabbit FITC-conjugated secondary anti-

https://doi.org/10.1021/acsomega.4c07393
ACS Omega 2024, 9, 49530−49538

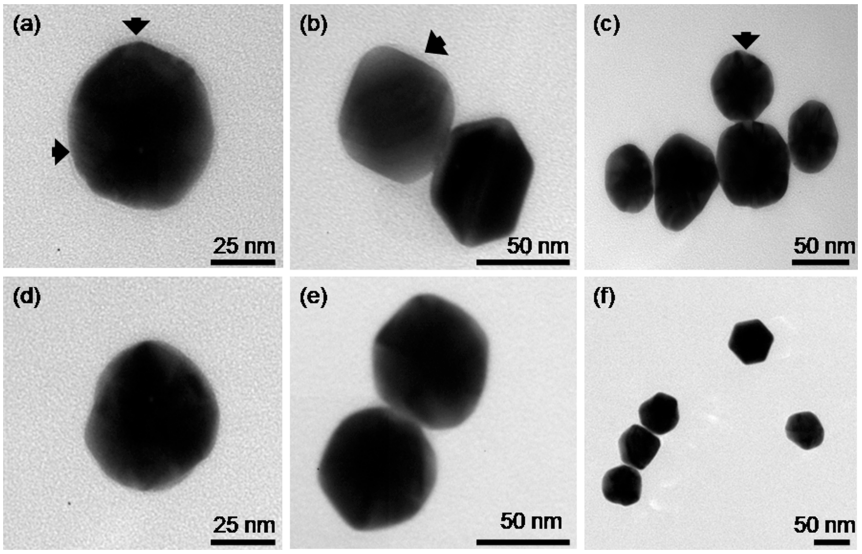

Figure 2. TEM images of CB-AuNPs (a−c) and PBS-AuNPs (d−f) at different magnifications.

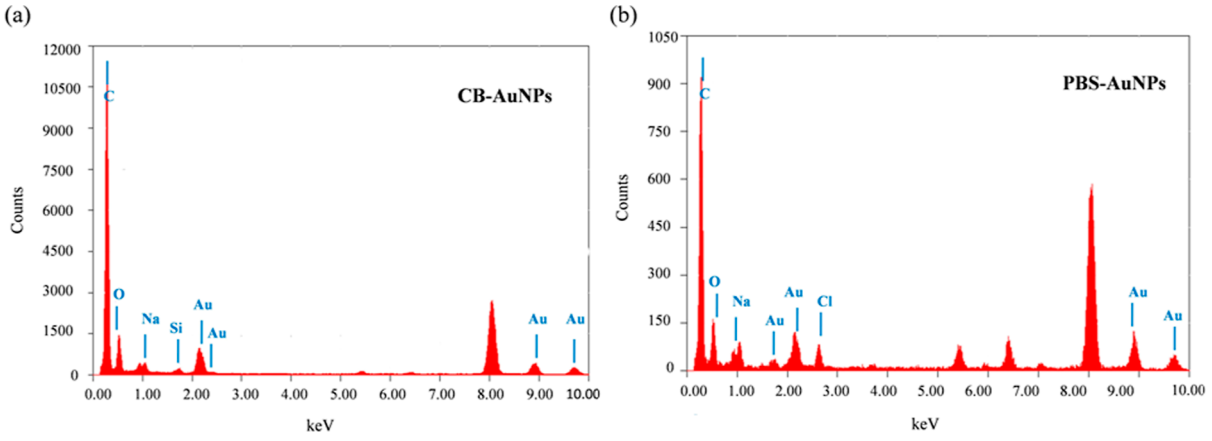

Figure 3. EDX spectra of CB-AuNPs (a) and PBS-AuNPs (b).

body (Sigma-Aldrich, 1:100) for signal detection. Negative controls were performed by omitting incubation with both AuNPs and anti-eNOS. Finally, the slides were mounted with mounting medium (Vectashield, Vector Laboratories, Burlingame, CA U.S.A.) and examined by laser scanning confocal microscopy (LSCM) (Leica, TCS SP8, Germany).

2.5. Laser Settings and Detection Parameters for LSCM. In this study, laser scanning confocal microscopy (LSCM) was used to require fluorescence and light-scattering images. The LSCM setup consisted of an upright microscope (Leica DM6000CS; Leica Microsystems GmbH, Wetzlar, Germany) with a Leica SP8-spectral scan-head. A 496 nm laser (Ar, 65 mW) was chosen for excitation to visualize eNOS labeled with fluorescein isothiocyanate (FITC). The photomultiplier (PMT) detection range was set from 506 to 750 nm to capture emitted fluorescence while minimizing scattered light interference. For imaging AuNPs distribution, light scattering images were acquired using a 561 nm laser within the SPR range. The PMT detection range was centered on the excitation wavelength with a 10 nm width to capture monochromatic scattered light. PMT sensitivity settings were standardized across all samples to ensure consistency.

2.6. Statistical Analysis. Analysis of fluorescence intensity (according to Lichocka and Schmelzer, 2014)[3] and plot profiles were performed using ImageJ software (ver. 1.46r, NIH, USA). Differences between the two groups (i.e., with and without AuNPs) were evaluated using the nonparametric Mann−Whitney *U* test. Statistical significance was set at $*p < 0.05$, $**p < 0.005$ and $***p < 0.0005$. Statistical analysis of the data was performed using GraphPad InStat software, version 3.10 for Windows.

3. RESULTS AND DISCUSSION

3.1. Characterization of Gold Nanoparticles. The gold nanoparticles (AuNPs) used in this study were characterized by transmission electron microscopy (TEM) to determine their average size and morphology. As shown in Figure 2 the average size of AuNPs ranges from 30 to 65 nm. The images in Figure 2a−c show that CB-AuNPs have a fine layer around them compared to uncoated PBS-AuNPs (Figure 2d−f).

To clarify the identity of these nanostructures, additional TEM studies were performed with EDX spectrum analysis (Figure 3). The EDX spectra of the two solutions reveal some differences in the peaks. For CB-AuNPs, a silicon (Si) peak is detected (Figure 3a), while for PBS-AuNPs, the EDX spectra, show a chlorine (Cl) peak (Figure 3b). The presence of Si peak in the EDX spectrum of CB-AuNPs probably refers to the presence of silicon in the form of a coating or compound, such

https://doi.org/10.1021/acsomega.4c07393
ACS Omega 2024, 9, 49530−49538

as silica (SiO_2), on the surface of the nanoparticles. The observed shell (Figure 2a–c) can be attributed to the silica coating on the AuNPs surface. Such an approach is commonly used during the synthesis or postsynthesis of AuNPs for various applications to enhance their stability and biocompatibility.[20−22]

Monodisperse nanoparticles exhibit distinct SPR properties. However, aggregation can alter these properties, leading to changes in the color of the dispersion. This can manifest as broadening and shifting of the SPR peak, resulting in a transition from red to blue in the dispersion.[23] In our experiment, the SPR band of the 50 nm AuNPs remained unaffected by the buffer solution (Figure 4). This band ranges from 400 to 600 nm, with a strong, narrow peak observed at approximately 537 nm, further supporting their monodispersity in the buffer solution.

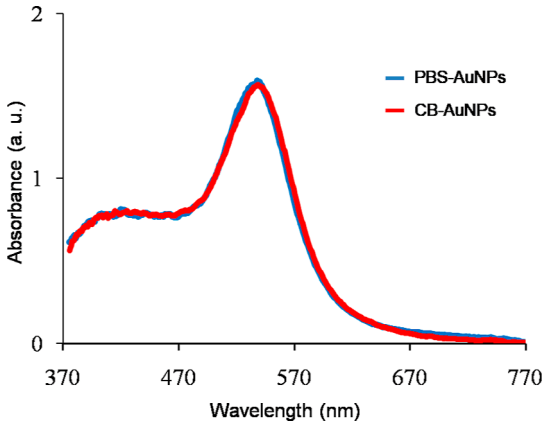

Figure 4. UV−visible absorption spectra of AuNPs dispersions.

The choice of buffer and stabilizer can significantly affect the zeta potential and thus the colloidal stability and behavior of nanoparticles in biological systems. Dynamic light scattering (DLS) measurements and zeta potential analysis (Table 1)

Table 1. Physicochemical Properties of Gold Nanoparticle Dispersions

gold nanoparticles dispersion	hydrodynamic diameter of AuNPs D_H(nm)	polydispersity index PDI	Zeta potential ζ (mv)
CB-AuNPs	57.03 ± 0.09	0.06 ± 0.01	−31.5 ± 0.624
PBS-AuNPs	51.91 ± 0.53	0.09 ± 0.01	−52.5 ± 0.987

confirm the stability of both types of AuNPs in their respective buffer solutions. AuNPs exhibit a low PDI of 0.09, significantly below 0.3. In addition, their zeta potentials exceed 30 mV in absolute value. These characteristics confirm the stability and suitability of the studied nanoparticles for a wide range of biological applications.[24,25] Interestingly, PBS-AuNPs have a more negative zeta potential (−50 mV) compared to CB-AuNPs (−35 mV), suggesting a higher degree of surface charge, which is consistent with our findings in EDX analysis. Thus, the presence of chloride (Cl^-) ions in PBS-AuNPs and silica in CB-AuNPs may contribute to the observed variations in zeta potential. These results highlight the significant influence of stabilizing agents and ions on the surface charge of nanoparticles.

3.2. Localization of eNOS. Histological examination of *P. annectens* gills, as illustrated in Figure 5, using hematoxylin and

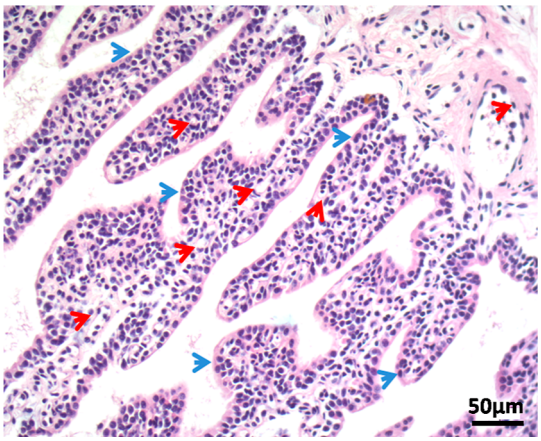

Figure 5. Histological features of the *P. annectens* gills stained with hematoxylin and eosin. Blue arrows indicate the respiratory epithelium, and red arrows indicate vessels.

eosin staining, revealed distinct morphological features. Specifically, it was observed that the secondary lamellae were surrounded by the respiratory epithelium (indicated by blue arrows) and exhibited robust vascularization (highlighted by red arrows).

As shown in Figure 6, LSCM images reveal a distinct localization pattern of eNOS within the gills of *P. annectens*,

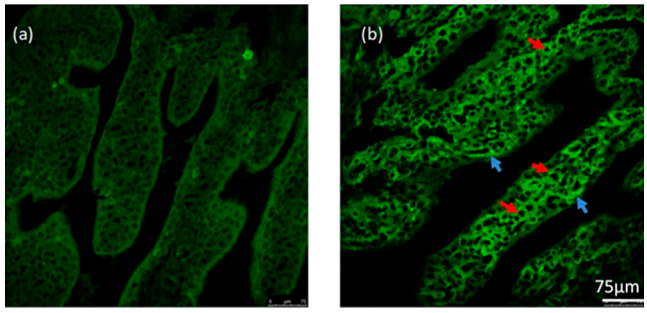

Figure 6. Immunolocalization of eNOS (b) in the gills of *P. annectens*. eNOS is predominantly localized in epithelial (blue arrows) and endothelial cells (red arrows). The negative control is shown in (a). An excitation wavelength of 496 nm was used to stimulate the fluorescence signal, which was subsequently detected in the range of 506−750 nm. Images were acquired using a 25× water immersion objective. The scale bar denotes 75 μm which is the same for both images.

with notable concentrations observed at the basal surface of epithelial cells and at the endothelial level (Figure 6b). The detectable fluorescence signal emanating from the eNOS protein was facilitated by fluorescence-labeled antibodies, specifically FITC, which emits in the range of approximately 490−630 nm, corresponding to the excitation wavelength of 496 nm used. The absence of immunoreactivity in the negative control was confirmed in Figure 6a. However, tissue autofluorescence, resulting from unbound FITC and autofluorescent molecules (such as flavins and collagen), contributed to the detected signal in the 500−700 nm range when excited by the 496 nm pump beam. This overlap creates a subtle distinction rather than a significant difference between

https://doi.org/10.1021/acsomega.4c07393
ACS Omega 2024, 9, 49530−49538

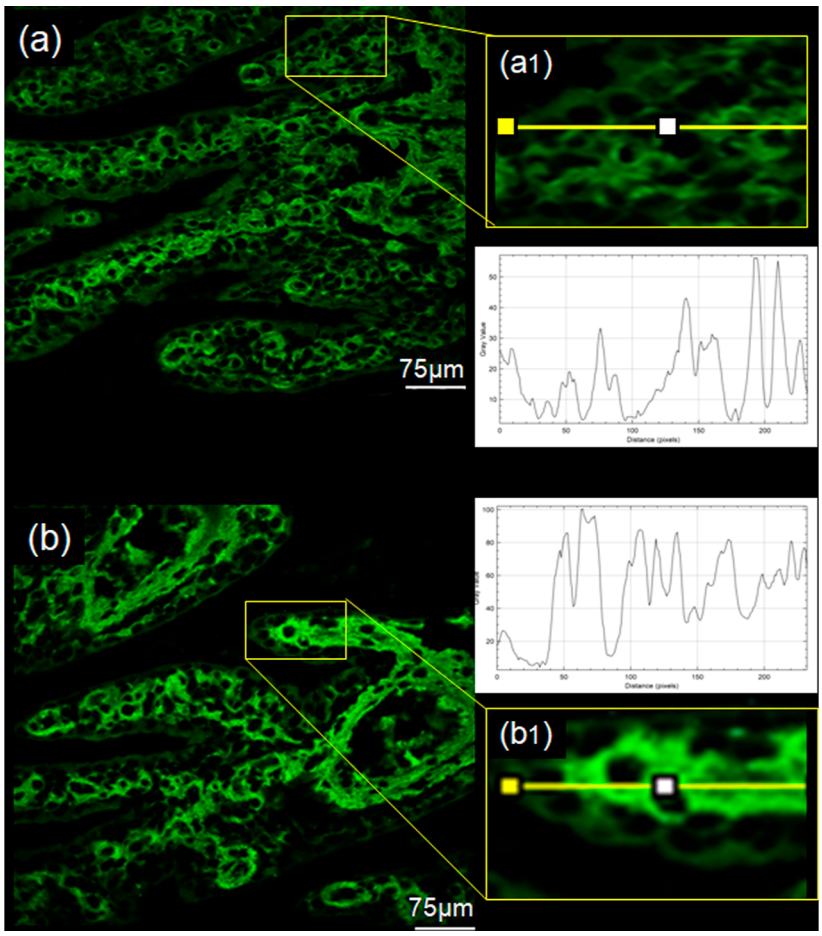

Figure 7. Immunolocalization of eNOS in the gills of *P. annectens* after incubation with 50 nm AuNPs, dispersed in citrate (a) and in PBS buffer solution (b). Under excitation at 496 nm, the emitted light is detected in the range of 506−750 nm. All images are observed with the 25× water immersion objective. Scale bar: 75 μm which is the same for images (a,b).

the desired signal from the target and the background (Figure 6b). To improve the quality of data obtained from LSCM images, it is critical to maximize the differentiation between these two signals.

3.3. Impact of AuNPs on the Immunolocalization of eNOS. Treatment of the sample with AuNPs results in increased image contrast (Figure 7a,b). The plot profile of fluorescence intensity in a limited area (Figure 7a1,b1) illustrates a distinct signal modulation, transitioning from enhanced fluorescence emitted by eNOS to autofluorescence quenching. This modulation is significantly more pronounced when tissues are treated with PBS-AuNPs (Figure 7a,a1) compared to CB-AuNPs (Figure 7b,b1).

To evaluate the effect of AuNPs on optical contrast, ratios (P/N) were calculated using the average fluorescence intensity values. The numerator (P) represents the average fluorescence intensity of eNOS within the gill epithelial cells, which serves as the positive signal. The denominator (N) represents the autofluorescence intensity, which serves as the negative signal. The P/N ratio was calculated for each image of AuNPs-treated tissues (Figure 7a,b) and compared with the ratio obtained from the image in Figure 7b corresponding to the AuNPs-untreated tissue (P/N = 1.664). The results of these calculated ratios are presented in a graph (Figure 8).

Figure 8 illustrates an increase in the measured ratio for images of tissues treated with AuNPs. The lowest ratio is observed when tissues are treated with CB-AuNPs, as shown in

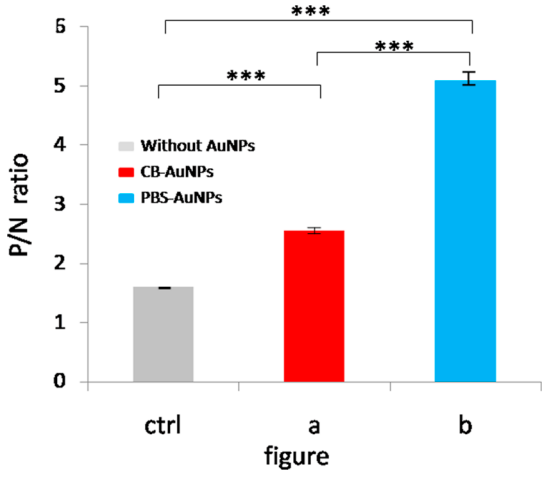

Figure 8. Graph of average intensity ratios of eNOS vs the average of the autofluorescence intensity (P/N ratio) in each image. Statistical differences were evaluated by the nonparametric Mann−Whitney *U* test (*p < 0.05, **p < 0.005 and ***p < 0.0005).

Figure 7b. In contrast, the most significant improvement in the contrast between positive and background signals is achieved when tissues are treated with AuNPs dispersed in PBS. In the current literature, several models have been developed to elucidate the interactions between fluorophores and gold.[10,11]

https://doi.org/10.1021/acsomega.4c07393
ACS Omega 2024, 9, 49530−49538

The efficiency of fluorescence quenching/enhancement depends on the fluorescence decay rate (Rfluo), the radiative decay rate (Rrad), and the nonradiative decay rate (Rnonrad).[12] Radiative decay occurs when the fluorophore emits a photon that returns to the ground state and is detected, contributing to fluorescence enhancement.[12] Conversely, nonradiative decay occurs when the excited photon is unable to return to the ground state due to processes such as intersystem transitions or heat dissipation leading to fluorescence quenching.[5] Moreover, several factors influence the manipulation of fluorescence and affect whether quenching or enhancement occurs. These factors include the distance between fluorophores and AuNPs, the orientation of the fluorophore relative to the AuNPs, influencing dipole−dipole interactions, and the spectral overlap between the fluorophore emission and AuNPs absorption spectra.[26,27]

In our studies, 50 nm AuNPs exhibited an SPR band ranging from 400 to 600 nm, with a peak at 537 nm, which overlapped with the emission spectrum of FITC (ranging from 490 to 630 nm, with a peak at 520 nm) (Figures 4 and 9), thus the spectral characteristics of both AuNPs and FITC meet the overlap requirement.

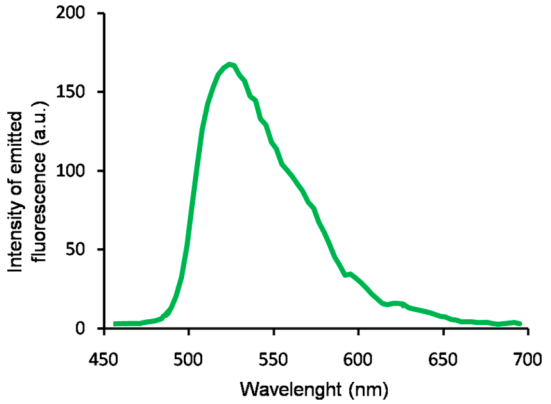

Figure 9. Fluorescence spectra of FITC bound to eNOS recorded in lambda scan mode. Emission is obtained under an excitation of 496 nm and it is detected in the 500−730 nm range.

The more pronounced enhancement of optical contrast observed in gills treated with PBS-AuNPs suggests a higher level of AuNPs attachment to cells when dispersed in PBS compared to CB. To further investigate the effect of varying the AuNPs solution on their biodistribution and attachment levels, additional imaging techniques were employed. These techniques provide insight into the spatial relationship between AuNPs and fluorophores, shedding light on their proximity, the nature of energy transfer, and attachment strength.

3.4. Light Scattering Images and ESEM Analysis of AuNPs Tissue Distribution. AuNPs with an average size of approximately 40 nm exhibit strong light scattering efficiency, which enhances their detection capabilities in various optical applications.[28,29] In our study, we employed confocal microscopy to combine fluorescence imaging with light scattering. This approach allows for better localization of AuNPs in tissues, as the strong light scattering helps distinguish AuNPs from target proteins (eNOS), providing a more comprehensive understanding of their biointeractions.

Fluorescence images of tissues treated with CB-AuNPs (Figure 10a) and PBS-AuNPs (Figure 10b) were complemented by corresponding light-scattering images (Figure 10c,d). Significantly, light-scattering images of tissues treated with PBS-AuNPs showed higher brightness, indicating a more homogeneous distribution of bright spots compared to tissues treated with CB-AuNPs, where limited, larger bright spots were observed.

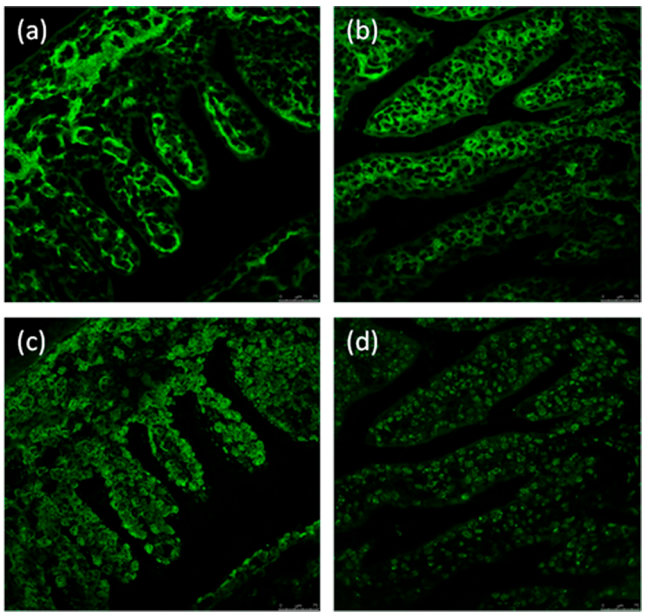

Figure 10. LSCM images of eNOS fluorescence in gill tissues after incubation with PBS-AuNPs (a) and CB-AuNPs (b). Under excitation at 496 nm, the emitted light is detected in the range of 506−750 nm. LSCM images of light scattering signal detected from the same tissues (top) in the range of 556−566 nm under the 561 nm (bottom) (c,d). The scale bar denotes 75 μm, which is the same for all images. Red arrows indicate the positions occupied by AuNPs when fluorescence images are acquired. Conversely, blue arrows indicate the locations of eNOS when light-scattering images are acquired allowing a clear distinction between the presence of AuNPs and the localization of eNOS depending on the imaging modality used.

To further investigate the nature of these microstructures and the biodistribution of AuNPs, samples were subjected to environmental scanning electron microscopy (ESEM) (Figure 11). The experimental SEM images revealed only a few small agglomerates of CB-AuNPs attached to tissues, suggesting that their attachment to cells occurred primarily through aggregation (Figure 11a,c,d). Conversely, a strong and homogeneous distribution of PBS-AuNPs within the tissue was observed by ESEM, indicating higher biocompatibility (Figure 11b,e,f). Confocal light scattering and ESEM images provided valuable insights into the spatial distribution of AuNPs and their specific localization pattern relative to eNOS, offering important information about the proximity of AuNPs to FITC fluorophores and their attachment to cells, which significantly affects optical contrast. Fluorescence images of tissues treated with PBS-AuNPs exhibited a more pronounced optical contrast enhancement due to their highly homogeneous biodistribution compared to tissues treated with CB-AuNPs. Our observations revealed the presence of AuNPs in close proximity to eNOS, indicating a distinct pattern in which AuNPs appear to avoid eNOS. This selective attachment behavior contributes to the intricate spatial distribution of AuNPs and their specific localization relative to eNOS, further

https://doi.org/10.1021/acsomega.4c07393
ACS Omega 2024, 9, 49530−49538

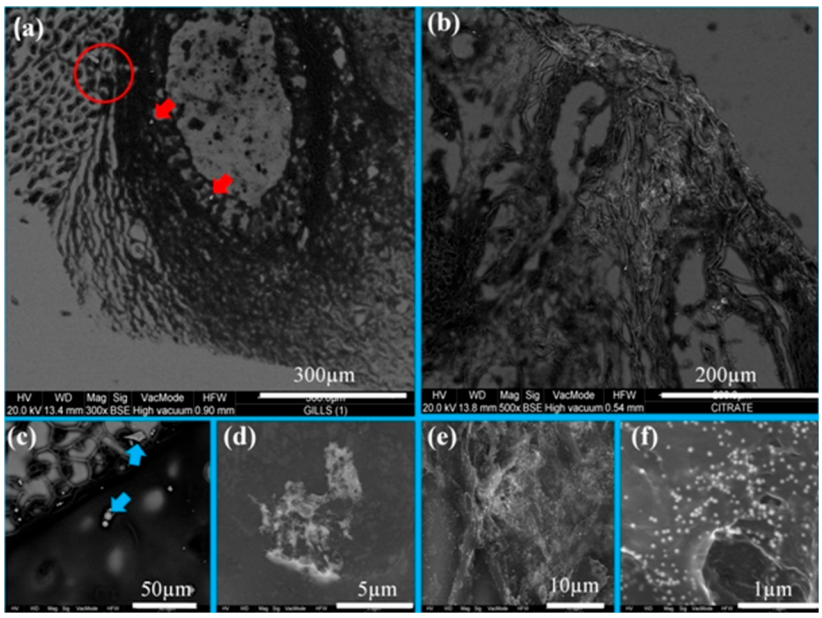

Figure 11. SEM image of gills in the presence of gold nanoparticles stabilized in CB (a) and PBS (b). Images (c,d) provide higher magnification views at the locations indicated by the red circle and arrow. Blue arrows indicate regions of strong light scattering and highlight different morphologies originating from citrate buffer. Images (e,f) provide detailed views of the SEM image in (b), showing the distribution and interaction of the nanoparticles within the gill tissue.

influencing optical contrast. Our results are consistent with existing literature, highlighting that AuNPs larger than 40 nm influence adjacent fluorophores through a dual mechanism, attributed to their efficient absorption and light scattering efficiencies.[28] At short distances, AuNPs interact with the fluorophore's electrons, leading to the quenching of fluorescence intensity. Specifically, quenching occurs at distances less than 10 nm due to Förster resonance energy transfer (FRET), a nonradiative energy transfer mechanism.[12,14] In contrast, at larger distances, the radiative process dominated by light scattering, associated with the plasmonic effects of AuNPs, contributes to fluorescence enhancement.[10−12] The observed enhancement in optical contrast in our study arises from this dual effect: efficient quenching of autofluorescence by FRET at close range and amplification of the eNOS signal through radiative energy transfer at a considerable distance.

The higher compatibility of PBS-AuNPs compared to CB-AuNPs during the immunofluorescence technique can be attributed to several factors, highlighting the intricate relationship between AuNP properties and the experimental conditions. The presence of the silica shell on CB-AuNPs in citrate buffer, as revealed by EDX analysis, suggests the presence of a protective layer that may restrict direct interactions with cellular components, resulting in limited attachment. Silica coatings are recognized for their ability to improve stability and minimize nonspecific interactions with biological molecules.[20−22] While our previous study revealed a unique interaction between AuNPs in citrate buffer with a silica shell and DNA,[24] suggesting an enhanced affinity, in the context of immunofluorescence, this protective nature of the silica shell could lead to limited attachment to cells, potentially impacting the overall compatibility of AuNPs with the biological tissue. Moreover, the SEM images of CB-AuNP-treated tissues (Figure 11a,c,d) highlight various morphologies that originated from the citrate buffer and exhibited strong light scattering, as indicated by the large bright spots in Figure 10d. These structures may result from the incompatibility of the buffer with the tissue, leading to weak attachment and aggregation of AuNPs. On the other hand, the detection of a chlorine peak in the EDX spectrum of AuNPs in PBS implies a different surface composition, making these nanoparticles more negatively charged. The literature suggests that negatively charged nanoparticles exhibit enhanced cellular uptake due to interactions with positively charged cell membranes.[30] Moreover, the immunofluorescence procedure itself may affect the compatibility of AuNPs with tissues. For example, the use of salt in TBS may alter the surface properties of AuNPs due to changes in ionic strength. While salts in TBS could potentially affect the behavior of AuNPs, the inherent negative charge and stability of AuNPs in PBS likely mitigate these effects, ensuring consistent behavior during immunofluorescence. Several studies have demonstrated aggregation induced by salt when AuNPs are in citrate solution,[19] highlighting the importance of selecting the appropriate nanoparticle and buffer solution for experimental techniques. This phenomenon was also observed in our study, as evidenced by SEM images of CB-AuNPs treated tissues, revealing distinct aggregates (Figure 10a,c,d). The aggregation of CB-AuNPs, exacerbated by the saline environment, could significantly affect their interaction with biological tissues. This aggregation may limit the dispersion and attachment of AuNPs, potentially contributing to the observed differences in compatibility compared to PBS-AuNPs. The combination of factors, including the protective silica shell on CB-AuNPs and the higher negative charge on the surface of PBS-AuNPs, along with the potential influence of the immunofluorescence procedure, contribute to the observed differences in compatibility. These properties not only enhance our understanding of the interactions between AuNPs and tissues but also open avenues for improving immunofluorescence techniques and expanding imaging applications, particularly in cases where AuNPs exhibit selective attachment patterns. Further investigations are

https://doi.org/10.1021/acsomega.4c07393
ACS Omega 2024, 9, 49530−49538

warranted to explore and optimize these properties for broader applications in imaging techniques.

4. CONCLUSION

In this study, we focused on investigating how AuNPs affect the localization of eNOS in gill tissue. Using citrate and PBS buffer solutions, we investigated their effect on the enhancement of optical contrast during immunofluorescence. Our results highlight the critical role of biocompatibility in achieving optimal contrast. The choice of AuNPs suspension solution proved to be critical; PBS-suspended AuNPs exhibited superior optical contrast enhancement compared to CB-suspended counterparts. The surface properties of AuNPs, particularly their charge characteristics influenced by the buffer solution, significantly affected compatibility with immunofluorescence techniques. In particular, PBS-AuNPs with a higher negative charge showed improved attachment and more homogeneous biodistribution in tissues. The protective silica shell on CB-AuNPs enhanced stability but resulted in limited attachment and compromised compatibility with immunofluorescence. Factors such as specific AuNP attachment mechanisms, which influence both fluorescence enhancement and quenching effects, contributed to the overall improvement in optical contrast. This study highlights the nuanced relationship between AuNPs and biological tissues, emphasizing the importance of strategic design and optimization of contrast agents for imaging applications. Future research should further investigate these interactions to advance imaging technologies, potentially leading to breakthroughs in contrast agent development. By exploiting the unique optical properties of AuNPs and understanding their interactions within biological systems, we can enhance contrast, improve sensitivity, and achieve more accurate visualization of target molecules in complex tissue environments.

AUTHOR INFORMATION

Corresponding Author

Souhaira Hbaieb − *Laboratoire de Recherche: Caractérisations, Applications et Modélisation de Matériaux, Université de Tunis El Manar, Faculté des Sciences de Tunis, Tunis 2092, Tunisia;* orcid.org/0000-0003-2565-5970; Phone: + 216 71 88 34 24; Email: souhaira.hbaieb@fst.utm.tn

Authors

Ramla Gary − *Laboratoire de Physique de la Matière Molle et de la Modélisation Electromagnétique, Faculté des Sciences de Tunis, Université de Tunis El Manar, Rommana 1068, Tunisie*

Manel Ben Salah − *Laboratoire de Physique de la Matière Molle et de la Modélisation Electromagnétique, Faculté des Sciences de Tunis, Université de Tunis El Manar, Rommana 1068, Tunisie*

Taoufik Soltani − *Laboratoire de Physique de la Matière Molle et de la Modélisation Electromagnétique, Faculté des Sciences de Tunis, Université de Tunis El Manar, Rommana 1068, Tunisie*

Patrizia Formoso − *Department of Pharmacy, Health and Nutritional Sciences, University of Calabria, 87036 Arcavacata di Rende, CS, Italy;* orcid.org/0000-0002-3568-1630

Complete contact information is available at: https://pubs.acs.org/10.1021/acsomega.4c07393

Author Contributions

All authors contributed to the study's conception and design. Material preparation, data collection and analysis were performed by [R.G.], [M.B.S.], [T.S.], [P.F.] and [S.H.]. The first draft of the manuscript was written by [R.G.] and all authors commented on previous versions of the manuscript. All authors read and approved the final manuscript.

Funding

The authors declare that no funds, grants, or other support were received during the preparation of this manuscript.

Notes

The authors declare no competing financial interest.

ACKNOWLEDGMENTS

We are grateful to Prof. Riccardo Barberi and Dr. Maria Penelope De Santo of the Physics Department of the University of Calabria for their support and provision of facilities. From the Biology Department, we thank Dr. Daniela Amelio and Dr. Filippo Garofalo for their help with tissue samples and statistical analyses, respectively. In addition, we appreciate the insightful feedback provided by Prof. Adel Ashi of the Physics Department at the Faculty of Science, Tunis El Manar, during the revision of this paper.

ABBREVIATIONS

AuNPs	gold nanoparticles
eNOS	endothelial-like nitric oxide synthase
PBS	phosphate buffer saline
SPR	surface plasmon resonance
FRET	Förster Resonance Energy Transfer
CTAB	hexadecyl trimethylammonium bromide
PSS	sodium polystyrenesulfonate
PDDAC	polyethylene diallyl dimethylammonium chloride
ZP	zeta potential
DH	hydrodynamic diameter
PDI	polydispersity index
TEM	transmission electron microscopy
EDX	X-ray energy dispersive spectroscopy
FESEM	field emission scanning electron microscope
PBS-AuNPs	AuNPs suspended in phosphate buffer saline
CB-AuNPs	AuNPs suspended in citrate buffer
TBS	tris-buffered saline
LSCM	laser scanning confocal microscopy
FITC	fluorescein isothiocyanate
Si	silicon
Cl	chlorine
SiO_2	silica
DLS	dynamic light scattering
Cl^-	chloride ion

REFERENCES

(1) Baschong, W.; Suetterlin, R.; Laeng, R. H. Control of Autofluorescence of Archival Formaldehyde-Fixed, Paraffin-Embedded Tissue in Confocal Laser Scanning Microscopy (CLSM). *J. Histochem. Cytochem.* **2001**, *49*, 1565−1571.

(2) Kittelberger, R.; Davis, P. F.; Stehbens, W. E. An Improved Immunofluorescence Technique for the Histological Examination of Blood Vessel Tissue. *Acta Histochem.* **1989**, *86*, 137−142.

(3) Lichocka, M.; Schmelzer, E. Subcellular Localization Experiments and FRET-FLIM Measurements in Plants. *J. Bioprotocol.* **2014**, *4*, 1−12.

(4) Buchwalow, I.; Samoilova, V.; Boecker, W.; Tiemann, M. Non-Specific Binding of Antibodies in Immunohistochemistry: Fallacies and Facts. *Sci. Rep.* **2011**, *1*, 28.
(5) Swierczewska, M.; Lee, S.; Chen, X. The Design and Application of Fluorophore−Gold Nanoparticle Activatable Probes. *Phys. Chem. Chem. Phys.* **2011**, *13*, 9929−9941.
(6) Aubin, J. E. Autofluorescence of Viable Cultured Mammalian Cells. *J. Histochem. Cytochem.* **1979**, *27*, 36−43.
(7) Benson, R. C.; Meyer, R. A.; Zaruba, M. E.; McKhann, G. M. Cellular Autofluorescence—Is It Due to Flavins? *J. Histochem. Cytochem.* **1979**, *27*, 44−48.
(8) Murphy, C. J.; Gole, A. M.; Stone, J. W.; Sisco, P. N.; Alkilany, A. M.; Goldsmith, E. C.; Baxter, S. C. Gold Nanoparticles in Biology: Beyond Toxicity to Cellular Imaging. *Acc. Chem. Res.* **2008**, *41*, 1721−1730.
(9) Bouché, M.; Hsu, J. C.; Dong, Y. C.; Kim, J.; Taing, K.; Cormode, D. P. Recent Advances in Molecular Imaging with Gold Nanoparticles. *Bioconjugate Chem.* **2020**, *31*, 303−314.
(10) Lakowicz, J. R. Radiative Decay Engineering 5: Metal-Enhanced Fluorescence and Plasmon Emission. *Anal. Biochem.* **2005**, *337*, 171−194.
(11) Lakowicz, J. R.; Shen, Y.; D'Auria, S.; Malicka, J.; Fang, J.; Gryczynski, I.; Gryczynski, Z. Radiative Decay Engineering. 2. Effects of Silver Island Films on Fluorescence Intensity, Lifetimes, and Resonance Energy Transfer. *Anal. Biochem.* **2002**, *301*, 261−277.
(12) Lakowicz, J. R. Radiative Decay Engineering: Biophysical and Biomedical Applications. *Anal. Biochem.* **2001**, *298*, 1−24.
(13) Kang, K. A.; Wang, J.; Jasinski, J. B.; Achilefu, S. Fluorescence Manipulation by Gold Nanoparticles: From Complete Quenching to Extensive Enhancement. *J. Nanobiotechnol.* **2011**, *9*, 16.
(14) Gary, R.; Amelio, D.; Garofalo, F.; Petriashvili, G.; De Santo, M. P.; Ip, Y. K.; Barberi, R. Endothelial-Like Nitric Oxide Synthase Immunolocalization by Using Gold Nanoparticles and Dyes. *Biomed. Opt. Express* **2015**, *6*, 4738−4748.
(15) Chithrani, B. D.; Chan, W. C. W. Elucidating the Mechanism of Cellular Uptake and Removal of Protein-Coated Gold Nanoparticles of Different Sizes and Shapes. *Nano Lett.* **2007**, *7*, 1542−1550.
(16) Gong, N.; Chen, S.; Jin, S.; Zhang, J.; Wang, P. C.; Liang, X. Effects of the Physicochemical Properties of Gold Nanostructures on Cellular Internalization. *Regener. Biomater.* **2015**, *2*, 273−280.
(17) Valente, K. P.; Suleman, A.; Brolo, A. G. Exploring Diffusion and Cellular Uptake: Charged Gold Nanoparticles in an in Vitro Breast Cancer Model. *ACS Appl. Biol. Mater.* **2020**, *3*, 6992−7002.
(18) Tan, K. F.; In, L. L. A.; Vijayaraj Kumar, P. Surface Functionalization of Gold Nanoparticles for Targeting the Tumor Microenvironment to Improve Antitumor Efficiency. *ACS Appl. Biol. Mater.* **2023**, *6*, 2944−2981.
(19) Jimmy Huang, P. J.; Yang, J.; Chong, K.; Ma, Q.; Li, M.; Zhang, F.; Moon, W. J.; Zhang, G.; Liu, J. Good's Buffers Have Various Affinities to Gold Nanoparticles Regulating Fluorescent and Colorimetric DNA Sensing. *Chem. Sci.* **2020**, *11*, 6795−6804.
(20) Chen, Y.; Frey, W.; Kim, S.; Kruizinga, P.; Homan, K.; Emelianov, S. Silica-Coated Gold Nanorods as Photoacoustic Signal Nanoamplifiers. *Nano Lett.* **2011**, *11*, 348−354.
(21) Chen, Y.; Frey, W.; Kim, S.; Homan, K.; Kruizinga, P.; Sokolov, K.; Emelianov, S. Enhanced Thermal Stability of Silica-Coated Gold Nanorods for Photoacoustic Imaging and Image-Guided Therapy. *Opt. Express* **2010**, *18*, 8867.
(22) Luke, G. P.; Bashyam, A.; Homan, K. A.; Makhija, S.; Chen, Y.; Emelianov, S. Y. Silica-Coated Gold Nanoplates as Stable Photoacoustic Contrast Agents for Sentinel Lymph Node Imaging. *Nanotechnology* **2013**, *24*, 455101.
(23) Kim, Y.; Johnson, R. C.; Hupp, J. T. Gold Nanoparticle-Based Sensing of "Spectroscopically Silent" Heavy Metal Ions. *Nano Lett.* **2001**, *1*, 165−167.
(24) Danaei, M.; Dehghankhold, M.; Ataei, S.; Hasanzadeh Davarani, F.; Javanmard, R.; Dokhani, A.; Khorasani, S.; Mozafari, M. R. Impact of Particle Size and Polydispersity Index on the Clinical Applications of Lipidic Nanocarrier Systems. *Pharmaceutics* **2018**, *10*, 57.
(25) Das, P.; Das, M. K. Chapter 4- Production and Physicochemical Characterization of Nanocosmeceuticals. *Nanocosmeceuticals* **2022**, 95−138.
(26) Weitz, D. A.; Garoff, S.; Gersten, J. I.; Nitzan, A. The Enhancement of Raman Scattering, Resonance Raman Scattering and Fluorescence from Molecules Adsorbed on a Rough Silver Surface. *J. Chem. Phys.* **1983**, *78*, 5324−5338.
(27) Gary, R.; Carbone, G.; Petriashvili, G.; De Santo, M. P.; Barberi, R. Detection of Gold Nanoparticles Aggregation Growth Induced by Nucleic Acid through Laser Scanning Confocal Microscopy. *Sensors* **2016**, *16*, 258.
(28) Jain, P. K.; Lee, K. S.; El-Sayed, I. H.; El-Sayed, M. A. Calculated Absorption and Scattering Properties of Gold Nanoparticles of Different Size, Shape, and Composition: Applications in Biological Imaging and Biomedicine. *J. Phys. Chem. B* **2006**, *110*, 7238−7248.
(29) Jans, H.; Liu, X.; Austin, L.; Maes, G.; Huo, Q. Dynamic Light Scattering as a Powerful Tool for Gold Nanoparticle Bioconjugation and Biomolecular Binding Studies. *J. Phys. Chem. B* **2009**, *81*, 9425−9432.
(30) Deng, Z. J.; Liang, M.; Toth, I.; Monteiro, M.; Minchin, R. F. Plasma Protein Binding of Positively and Negatively Charged Polymer-Coated Gold Nanoparticles Elicits Different Biological Responses. *Nanotoxicology* **2013**, *7*, 314−322.

https://doi.org/10.1021/acsomega.4c07393
ACS Omega 2024, 9, 49530−49538